Computational and Applied Mathematics (2018) 37:6132–6151
https://doi.org/10.1007/s40314-018-0676-5

Magnetohydrodynamic double-diffusive natural convection for nanofluid within a trapezoidal enclosure

T. R. Mahapatra[1] · **Bikash C. Saha**[1] · **Dulal Pal**[1]

Received: 13 October 2017 / Revised: 12 May 2018 / Accepted: 5 July 2018 / Published online: 20 July 2018

Abstract

Double-diffusive natural convection flow in a trapezoidal cavity with various aspect ratios in the presence of water-based nanofluid and applied magnetic field in the direction perpendicular to the bottom and top parallel walls is investigated. The bottom and top parallel walls are considered to be insulated, whereas left and right walls are assumed to be uniformly heated and cold, respectively. The numerical computation is carried out to find the streamlines, isotherms, isoconcentrations, average Nusselt number, and average Sherwood number. This study is done for various values of Rayleigh number ($10^5 \leq Ra \leq 10^7$), Hartmann number ($0 \leq Ha \leq 120$), various aspect ratios ($0.5 \leq A \leq 2$), the solid volume fraction ($0 \leq \varphi \leq 0.1$), and the inclination angle of cavity (ϕ). It is found that the strength of vortex decreases/increases as the magnetic field parameter/aspect ratio increases. It is also found that increase in the Rayleigh number causes natural convection due to the increase in the buoyancy forces. In nanofluid, mass transfer ratio is more effective than base fluid.

Keywords Trapezoidal enclosure · Natural convection flow · Magnetic field · Nanofluid · Aspect ratio of a cavity

Mathematics Subject Classification 65N06 · 65N22 · 76D05 · 76W05 · 76R10 · 76R50

List of symbols

x, y	Distance along x and y coordinate, m
X, Y	Dimensionless distance along x and y coordinate
u, v	x and y component of velocity, m s^{-1}
U, V	x and y component of dimensionless velocity

Communicated by Corina Giurgea.

✉ T. R. Mahapatra
trmahapatra@yahoo.com

Bikash C. Saha
bcsaha87@gmail.com

Dulal Pal
dulalp123@rediffmail.com

[1] Department of Mathematics, Visva-Bharati (A Central University), Santiniketan, West Bengal 731 235, India

g	Acceleration due to gravity, m s^{-2}
T, T_h, T_c	Temperature of fluid, hot and cold wall, K
p	Pressure, Pa
P	Dimensionless pressure
L	Length of the base of the trapezoidal cavity, m
D	Mass diffusivity, m^2 s^{-1}
C_p	Specific heat, J kg^{-1} K^{-1}
k	Thermal conductivity, W m^{-1} K^{-1}
n	Normal vector to the plane
Nu, $\overline{Nu}$	Local and average Nusselt number
Pr	Prandtl number
Ra	Rayleigh number
B_0	Magnetic field strength
Ha	Hartmann number
Le	Lewis number
c_h, c_c	Concentration of hot and cold walls
Sh, $\overline{Sh}$	Local and average Sherwood number
N	Buoyancy ratio
c	Concentration
C	Dimensionless concentration

Greek symbols

θ	Dimensionless temperature
ϕ	Inclination angle with positive direction of x axis
β	Volume expansion coefficient, K^{-1}
μ	Dynamic viscosity, kg m^{-1} s^{-1}
ν	Kinematic viscosity, m^2 s^{-1}
ψ	Dimensionless stream function
ρ	Density, kg m^{-3}
σ	Electrical conductivity, kg^{-1} m^{-3} s^3 A^2
α	Thermal diffusivity, m^2 s^{-1}
φ	Volume fraction of the nanoparticle

Subscripts

p	Solid particles
r	Right wall
l	Left wall
nf	Nanofluid
f	Base fluid

1 Introduction

Fluid flow of water-based nanofluids, and heat and mass transfer due to natural convection induced by applied magnetic field in a trapezoidal enclosure have practical importance in many engineering applications and geophysical problems. Effects of magnetic field and aspect ratio of a cavity occur in a wide range of scientific field, such as geology, biology, oceanography, astrophysics, and chemical processes. These include solar collectors, nuclear reactors, solar ponds, electronic cooling, geothermal reservoirs, and chemical processing equipments.

During past few decades, studies on natural convection in a trapezoidal cavities have been under taken by many researchers. Lyiean et al. (1980) studied rate of heat transfer in natural convection within a trapezoidal cavity. Basak et al. (2009) investigated flow due to natural convection in a trapezoidal enclosure filled with porous medium. Peric (1993) examined natural convection within a trapezoidal cavity with various aspect ratios. On the other hand, some of the important studies on natural convection of nanofluid in a various enclosure can be found in Sheremet et al. (2016), Mahmoodi (2011), Ghasemi et al. (2011), Mahmoudi and Abu-Nada (2013), Das and Oha (2009), Corcione (2010), and Nasrin and Parvin (2012). Sheremet et al. (2016) investigated numerically entropy generation due to natural convection in a square cavity filled with nanofluid with hot solid object inserted by cooling the top wall and left bottom corners. Mahmoodi (2011) studied heat transfer in free convection and fluid flow in a square cavity containing nanofluid in the presence of an inside heater. Ghasemi et al. (2011) numerically examined natural convection in a square cavity filled with a water–Al_2O_3 nanofluid in the presence of horizontally applied magnetic field. Mahmoudi and Abu-Nada (2013) studied combined effect of the magnetic field and nanofluids on natural convection within a square cavity. Das and Oha (2009) examined heat transfer in natural convection within a partially heated and cooled square cavity filled with nanofluids for various thermal boundary conditions. Corcione (2010) studied buoyancy-driven heat transfer in rectangular cavity with differentially heated side walls. Nasrin and Parvin (2012) numerically investigated buoyancy-driven flow and heat transfer in a trapezoidal cavity filled with nanofluid for different temperature conditions.

Apart from these studies, there have been considerable interest to study double-diffusive natural convection of base fluid and nanoparticles in enclosure of different shapes. Chen et al. (2016) studied double-diffusive natural convection in a square enclosure filled with water-based SiO_2 nanofluid. They observed that the influences of addition of nanoparticles into base fluid are quite different between the laminar and turbulent regimes. Mahapatra et al. (2013) studied magnetohydrodynamic-mixed convection flow in an inclined enclosure with thermal radiation and heat generation. Dastmalchi et al. (2015) studied double-diffusive natural convection in a porous square cavity filled with nanofluid. It was performed for several physical conditions with various values of temperature difference between the hot and cold walls, bulk volume fraction of nanoparticles, and porosity. Tofaneli and de Lemos (2009) studied double-diffusive turbulent natural convection in a porous square cavity with opposing temperature and concentration gradients. Chen et al. (2012) studied numerically double-diffusive turbulent natural convection in a square cavity by LES-based lattice Boltzmann model with Rayleigh number up to 10^{11} and buoyancy ratio varying from 0.1 to 2. Parvin et al. (2013) investigated the effect of natural convection parameter Rayleigh number on double-diffusive natural convection in a partially heated square cavity filled with water-based Al_2O_3 nanofluid. Esfahani and Bordbar (2011) studied double-diffusive natural convection in a square cavity filled with different nanofluids. They observed that increasing the values of nanoparticle volume fraction, the flow strength will be reduced in the cavity. Arani et al. (2014) investigated double-diffusive natural convection of Al_2O_3–water nanofluid in a square cavity with partially heated side walls. Sivasankaran and Kandaswamy (2006) examined double-diffusive natural convection of water in a partitioned enclosure with temperature-dependent species diffusivity. Arefmanesh et al. (2015) studied the mixed convection fluid flow and heat transfer in a trapezoidal cavity filled with nanofluids by considering the effect of Brownian motion. Nayak et al. (2015) numerically studied mixed convection and entropy generation of nanofluid in a differentially heated skewed enclosure. A numerical work was carried out by Teamah and Shehata (2016) to study the effect of magnetic field on double diffusion within a trapezoidal cavity. Uddin et al. (2016) investigated unsteady double diffusion mixed

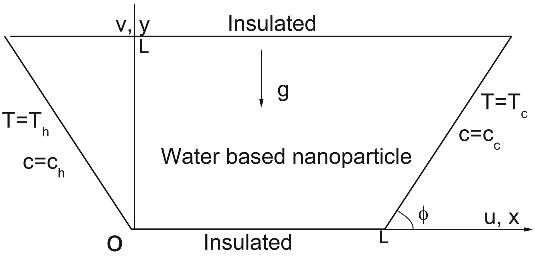

Fig. 1 Schematic diagram of the physical domain

convection flow due to uniform and nonuniform heating at the bottom side wall in lid-driven trapezoidal cavity in the presence of magnetic field . A few investigations on stagnation-point flow of nanofluids appear in the works of earlier researchers (Pal et al. 2014; Pal and Mandal 2015; Pal et al. 2015).

Over the years, the primitive variable and stream function–vorticity formulation are used to compute incompressible viscous flows governed by the Navier–Stokes equations. The primitive variable formulation is difficult because of the presence of the pressure term in the governing equations, whereas the stream function–vorticity formulation is difficult, because the vorticity prescribed on the boundaries. Due to these facts, the biharmonic pure stream function form of the Navier–Stokes equations, which eliminates the need to compute both pressure and vorticity, is emerging as an attractive alternative (Gupta 1975; Gupta and Kalita 2005; Kalita and Sen 2012; Pandit 2008). It is worth mentioning here that we have adopted this biharmonic strategy in our formulation.

The prime objective of this paper is to analyze numerically the flow and thermal characteristics of water-based nanofluid confined within a trapezoidal cavity by considering heating of side walls in presence of magnetic field. We also want to study the effects of aspect ratio of a trapezoidal cavity on heat and mass transfer with various angles and nanoparticles. The numerical results for streamline contours, isotherms, isoconcentrations, average Nusselt number, and average Sherwood number are presented graphically. It is found that the conduction mode of heat transfer dominates the convection mode with increase in the magnetic field. It is interesting to find that, due to the growth of number of the nanoparticles, effective viscosity is more prominent than the growth of the effective thermal conductivity at a large aspect ratio.

This paper is organized in five sections. Section 2 deals with the mathematical formulation, Sect. 3 provides numerical solution procedure, and Sect. 4 gives numerical results and discussion. In Sect. 5, we summarize the results of the present investigation.

2 Mathematical formulation

2.1 Governing equations and boundary conditions

Consider the trapezoidal cavity filled with water-based nanofluid and a laminar flow is initiated due to the imposition of different kinds of temperatures and concentration conditions at the different walls under the influence of magnetic field applied in the horizontal direction. The displacement current, induced magnetic field, dissipation, and Joule heating are neglected. This is justified for the flow where magnetic Reynolds number is small. The physical domain of a trapezoidal cavity is shown in Fig. 1 with the left and the right wall inclined at angles $(\pi - \phi)$ and ϕ, with x-axis. The governing equations for steady two-dimensional natural convection flow of a water-based nanofluid in dimensional form can be written as:

$$\frac{\partial u}{\partial x}+\frac{\partial v}{\partial y}=0, \tag{1}$$

$$u\frac{\partial u}{\partial x}+v\frac{\partial u}{\partial y}=-\frac{1}{\rho_{\mathrm{nf}}}\frac{\partial p}{\partial x}+\nu_{\mathrm{nf}}\left[\frac{\partial^2 u}{\partial x^2}+\frac{\partial^2 u}{\partial y^2}\right]-\frac{\sigma_{\mathrm{nf}}\ B_0^2\ u}{\rho_{\mathrm{nf}}}, \tag{2}$$

$$\begin{aligned}u\frac{\partial v}{\partial x}+v\frac{\partial v}{\partial y}&=-\frac{1}{\rho_{\mathrm{nf}}}\frac{\partial p}{\partial y}+\nu_{\mathrm{nf}}\left[\frac{\partial^2 v}{\partial x^2}+\frac{\partial^2 v}{\partial y^2}\right]\\&\quad+\frac{g(\rho\beta_{\mathrm{T}})_{\mathrm{nf}}}{\rho_{\mathrm{nf}}}(T-T_{\mathrm{c}})-\frac{g(\rho\beta_{\mathrm{S}})_{\mathrm{nf}}}{\rho_{\mathrm{nf}}}(c-c_{\mathrm{c}}),\end{aligned} \tag{3}$$

$$u\frac{\partial T}{\partial x}+v\frac{\partial T}{\partial y}=\alpha_{\mathrm{nf}}\left[\frac{\partial^2 T}{\partial x^2}+\frac{\partial^2 T}{\partial y^2}\right], \tag{4}$$

$$u\frac{\partial c}{\partial x}+v\frac{\partial c}{\partial y}=D\left[\frac{\partial^2 c}{\partial x^2}+\frac{\partial^2 c}{\partial y^2}\right]. \tag{5}$$

The boundary conditions of the physical problem are as follows: in all the four walls, no slip condition prevails. This condition gives $u=0,\ v=0$ at the four walls. The bottom and top walls are adiabatic ($\frac{\partial T}{\partial y}=0$), whereas left wall is hot ($T=T_{\mathrm{h}}$) and right wall is cold ($T=T_{\mathrm{c}}$). The concentration gradients at the bottom and top walls are considered to be zero and concentration at left and right walls are assumed constants which are c_{h} and c_{c}, respectively. Using the dimensionless quantities:

$$X=\frac{x}{L},\ Y=\frac{y}{L},\ U=\frac{uL}{\alpha_{\mathrm{f}}},\ V=\frac{vL}{\alpha_{\mathrm{f}}},\ C=\frac{c-c_{\mathrm{c}}}{c_{\mathrm{h}}-c_{\mathrm{c}}},\theta=\frac{T-T_{\mathrm{c}}}{T_{\mathrm{h}}-T_{\mathrm{c}}},\ P=\frac{pL^2}{\rho_{\mathrm{nf}}\alpha_{\mathrm{f}}^2},$$

$$Pr=\frac{\nu_{\mathrm{f}}}{\alpha_{\mathrm{f}}},\ Ha=\sqrt{\frac{\rho_{\mathrm{f}}}{\mu_{\mathrm{f}}}}\,B_0L,\ Le=\frac{\alpha_{\mathrm{f}}}{D},\ Ra=\frac{g\ \beta_{\mathrm{f}}(T_{\mathrm{h}}-T_{\mathrm{c}})L^3}{\nu_f\alpha_{\mathrm{f}}},\ N=\frac{\beta_{\mathrm{S}}(c_{\mathrm{h}}-c_{\mathrm{c}})}{\beta_{\mathrm{T}}(T_{\mathrm{h}}-T_{\mathrm{c}})}.$$

The governing Eqs. (1)–(5) reduce to dimensionless form:

$$\frac{\partial U}{\partial X}+\frac{\partial V}{\partial Y}=0, \tag{6}$$

$$U\frac{\partial U}{\partial X}+V\frac{\partial U}{\partial Y}=-\frac{\partial P}{\partial X}+\frac{\mu_{\mathrm{nf}}}{\rho_{\mathrm{nf}}\alpha_{\mathrm{f}}}\left[\frac{\partial^2 U}{\partial X^2}+\frac{\partial^2 U}{\partial Y^2}\right]-\frac{\sigma_{\mathrm{nf}}\rho_{\mathrm{f}}}{\sigma_{\mathrm{f}}\rho_{\mathrm{nf}}}Ha^2\ U, \tag{7}$$

$$U\frac{\partial V}{\partial X}+V\frac{\partial V}{\partial Y}=-\frac{\partial P}{\partial Y}+\frac{\mu_{\mathrm{nf}}}{\rho_{\mathrm{nf}}\alpha_{\mathrm{f}}}\left[\frac{\partial^2 V}{\partial X^2}+\frac{\partial^2 V}{\partial Y^2}\right]+\frac{(\rho\beta)_{\mathrm{nf}}}{\rho_{\mathrm{nf}}\beta_{\mathrm{f}}}\ Ra\ Pr\ (\theta-N\ C), \tag{8}$$

$$U\frac{\partial \theta}{\partial X}+V\frac{\partial \theta}{\partial Y}=\frac{\alpha_{\mathrm{nf}}}{\alpha_{\mathrm{f}}}\left[\frac{\partial^2 \theta}{\partial X^2}+\frac{\partial^2 \theta}{\partial Y^2}\right], \tag{9}$$

$$U\frac{\partial C}{\partial X}+V\frac{\partial C}{\partial Y}=\frac{1}{Le}\left[\frac{\partial^2 C}{\partial X^2}+\frac{\partial^2 C}{\partial Y^2}\right]. \tag{10}$$

The dimensionless initial boundary conditions are as follows:

$$\begin{aligned}&U=0,\ V=0\quad\text{at all the four walls,}\\&\frac{\partial\theta}{\partial Y}=0=\frac{\partial C}{\partial Y}\quad\text{at the bottom and top walls,}\\&\theta=1=C\quad\text{at the left wall,}\\&\theta=0=C\quad\text{at the right wall.}\end{aligned}$$

We introduce stream function (ψ) and vorticity (ω) in the following manner:

$$U = \frac{\partial \psi}{\partial Y}, \quad V = -\frac{\partial \psi}{\partial X}, \quad \omega = \frac{\partial V}{\partial X} - \frac{\partial U}{\partial Y}. \tag{11}$$

Using Eq. (6) and eliminating P from Eqs. (7) and (8), we get

$$P_1\left[\frac{\partial^2 \omega}{\partial X^2} + \frac{\partial^2 \omega}{\partial Y^2}\right] - \left[U\frac{\partial \omega}{\partial X} + V\frac{\partial \omega}{\partial Y}\right] + P_2\frac{\partial U}{\partial Y} + P_3\left(\frac{\partial \theta}{\partial X} - N\frac{\partial C}{\partial X}\right) = 0, \tag{12}$$

where $P_1,\ P_2,\ P_3$ are defined in Appendix. Combining three equations in Eq. (11), we get the governing equation for ψ as

$$\frac{\partial^2 \psi}{\partial X^2} + \frac{\partial^2 \psi}{\partial Y^2} = -\omega. \tag{13}$$

2.2 Thermophysical properties of the nanofluid

The effective density, the heat capacity, thermal expansion coefficient, and electrical conductivity of the nanofluid (see, Kefayati 2015; Xuan and Roetzel 2000) are given by the following relations:

$$\rho_{\mathrm{nf}} = (1-\varphi)\rho_{\mathrm{f}} + \varphi\rho_{\mathrm{p}}, \quad (\rho C_{\mathrm{p}})_{\mathrm{nf}} = (1-\varphi)(\rho C_{\mathrm{p}})_{\mathrm{f}} + \varphi(\rho C_{\mathrm{p}})_{\mathrm{p}},$$
$$(\rho\beta)_{\mathrm{nf}} = (1-\varphi)(\rho\beta)_{\mathrm{f}} + \varphi(\rho\beta)_{\mathrm{p}}, \quad \sigma_{\mathrm{nf}} = \sigma_f\left(1 + \frac{3(\zeta-1)\varphi}{(\zeta+2)-(\zeta-1)\varphi}\right),$$

respectively, where φ is the volume fraction of the nanoparticle, $\zeta = \sigma_{\mathrm{p}}/\sigma_{\mathrm{f}}$, and the subscripts f and p refer to the base fluid and nanoparticle, respectively. Thermal diffusivity of the nanofluid is $\alpha_{\mathrm{nf}} = k_{\mathrm{nf}}/(\rho C_{\mathrm{p}})_{\mathrm{nf}}$, where k_{nf} is effective thermal conductivity and is given by the following expression:

$$k_{\mathrm{nf}} = k_{\mathrm{f}}\left[\frac{k_{\mathrm{p}} + 2k_f - 2\varphi(k_{\mathrm{f}} - k_{\mathrm{p}})}{k_{\mathrm{p}} + 2k_{\mathrm{f}} + \varphi(k_{\mathrm{f}} - k_{\mathrm{p}})}\right].$$

Here, k_{f} and k_{p} are thermal conductivity of the base fluid and nanoparticle, respectively. The effective viscosity of the nanofluid is obtained from the Brinkman model (see, Brinkman 1952) which is expressed by

$$\mu_{\mathrm{nf}} = \mu_{\mathrm{f}}(1-\varphi)^{-2.5},$$

where μ_{f} is the viscosity of the base fluid. The thermophysical properties of the base fluid (pure water) and the solid particle are given in Table 1.

2.3 Coordinate transformation and biharmonic formulation

Application of the boundary conditions at the various boundaries is a difficult task. The prescription of conditions at boundaries not conforming to the coordinate lines leads to severe interpolation errors. For this reason, a transformation is introduced to map irregular physical domain to square computational domain. In this study, the physical (X, Y) plane is transformed into the computational (ξ, η) plane using the mapping:

$$\xi = \frac{X + Y\cot\phi}{1 + 2Y\cot\phi}, \quad \eta = \frac{Y}{A},$$

Table 1 Thermophysical properties of the base fluid (pure water) and nanoparticle

Properties	Pure water	$Al_2 O_3$	Cu	Ag	TiO_2
C_p (J kg^{-1} K^{-1})	4179	765	385	235	686.2
k (W m^{-1} K^{-1})	0.623	40	400	429	8.9538
ρ (kg m^{-3})	997.1	3970	8933	10500	4250
β (K^{-1})	21×10^{-5}	0.8×10^{-5}	1.67×10^{-5}	1.8×10^{-5}	0.9×10^{-5}
σ (kg^{-1} m^{-3} s^3 A^2)	0.05	3.69×10^7	5.69×10^7	6.30×10^7	2.38×10^6
μ (kg m^{-1} s^{-1})	0.001003	–	–	–	–
α (m^2 s^{-1})	0.143×10^{-6}	–	–	–	–

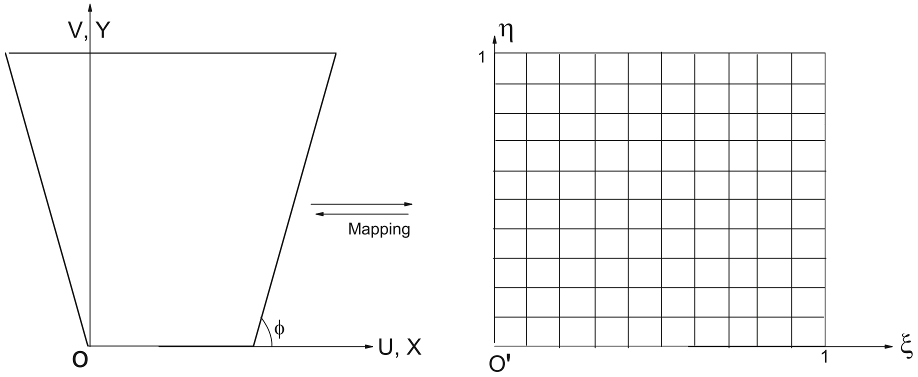

Fig. 2 Mapping of the trapezoidal domain to a square domain

where A is aspect ratio of a cavity. This mapping is employed the physical trapezoidal flow domain to computational square flow domain which is shown in Fig. 2. Equations (9), (10), (12), and (13) are transformed to

$$P_4 F \frac{\partial^2 \theta}{\partial \xi^2} + E P_4 \frac{\partial^2 \theta}{\partial \xi \partial \eta} + \frac{P_4}{A^2} \frac{\partial^2 \theta}{\partial \eta^2} = -B \frac{\partial \theta}{\partial \xi} + \frac{V}{A} \frac{\partial \theta}{\partial \eta}, \tag{14}$$

$$F \frac{\partial^2 C}{\partial \xi^2} + E \frac{\partial^2 C}{\partial \xi \partial \eta} + \frac{1}{A^2} \frac{\partial^2 C}{\partial \eta^2} = -Le\ P_6 \frac{\partial C}{\partial \xi} + \frac{Le\ V}{A} \frac{\partial C}{\partial \eta}, \tag{15}$$

$$P_1 F \frac{\partial^2 \omega}{\partial \xi^2} + P_1 E \frac{\partial^2 \omega}{\partial \xi \partial \eta} + \frac{P_1}{A^2} \frac{\partial^2 \omega}{\partial \eta^2} + M \frac{\partial \omega}{\partial \xi} - \frac{V}{A} \frac{\partial \omega}{\partial \eta}$$
$$+ P_3 G \left(\frac{\partial \theta}{\partial \xi} - N \frac{\partial C}{\partial \xi} \right) + P_2 \left(\frac{EA}{2} \frac{\partial U}{\partial \xi} + \frac{1}{A} \frac{\partial U}{\partial \eta} \right) = 0, \tag{16}$$

$$F \frac{\partial^2 \psi}{\partial \xi^2} + E \frac{\partial^2 \psi}{\partial \xi \partial \eta} + \frac{1}{A^2} \frac{\partial^2 \psi}{\partial \eta^2} + H \frac{\partial \psi}{\partial \xi} = -\omega, \tag{17}$$

where

$$U = \left(\frac{EA}{2} \psi_\xi \right) + \left(\frac{1}{A} \psi_\eta \right), V = -\left(G \psi_\xi \right). \tag{18}$$

Eliminating ω from Eq. (16), with the help of Eq. (17), we get

$$\begin{aligned}&P_1F^2\frac{\partial^4\psi}{\partial\xi^4}+2P_1EF\frac{\partial^4\psi}{\partial\xi^3\partial\eta}+T_5\frac{\partial^4\psi}{\partial\xi^2\partial\eta^2}+\frac{2P_1E}{A^2}\frac{\partial^4\psi}{\partial\xi\partial\eta^3}+\frac{P_1}{A^4}\frac{\partial^4\psi}{\partial\eta^4}\\&+T_1\frac{\partial^3\psi}{\partial\xi^3}+T_2\frac{\partial^3\psi}{\partial\xi^2\partial\eta}+T_3\frac{\partial^3\psi}{\partial\xi\partial\eta^2}\\&-\frac{V}{A^3}\frac{\partial^3\psi}{\partial\eta^3}+T_4\frac{\partial^2\psi}{\partial\xi^2}+T_6\frac{\partial^2\psi}{\partial\xi\partial\eta}+T_7\frac{\partial\psi}{\partial\xi}\\&-P_3G\left(\frac{\partial\theta}{\partial\xi}-N\frac{\partial C}{\partial\xi}\right)-P_2\left(\frac{EA}{2}\frac{\partial U}{\partial\xi}+\frac{1}{A}\frac{\partial U}{\partial\eta}\right)=0,\end{aligned}\tag{19}$$

which is biharmonic equation in stream function–velocity formulation, where $B,\ E,\ F,\ G,\ H,\ M,\ P_4, P_6,\ T_1,\ T_2,\ T_3,\ T_4,\ T_5,\ T_6,$ and T_7 are defined in the Appendix.

2.4 Nusselt number

The heat transfer rate in terms of the local Nusselt number (Nu) is defined by

$$Nu=-\frac{k_{\mathrm{nf}}}{k_{\mathrm{f}}}\frac{\partial\theta}{\partial n},$$

where n is the normal direction on a plane. The local Nusselt number at right wall (Nu_{r}) and left wall (Nu_{l}) is defined as follows:

$$Nu_{\mathrm{r}}=-\sin\phi\frac{k_{\mathrm{nf}}}{k_{\mathrm{f}}}\frac{\partial\theta}{\partial X}+\cos\phi\frac{k_{\mathrm{nf}}}{k_{\mathrm{f}}}\frac{\partial\theta}{\partial Y},\ Nu_{\mathrm{l}}=\sin\phi\frac{k_{\mathrm{nf}}}{k_{\mathrm{f}}}\frac{\partial\theta}{\partial X}+\cos\phi\frac{k_{\mathrm{nf}}}{k_{\mathrm{f}}}\frac{\partial\theta}{\partial Y}.$$

The average Nusselt number at left wall ($\overline{Nu_{\mathrm{l}}}$) and right ($\overline{Nu_{\mathrm{r}}}$) walls are given by

$$\overline{Nu_{\mathrm{l}}}=\frac{\sin\phi}{A}\int_0^{\frac{A}{\sin\phi}}Nu_{\mathrm{l}}\mathrm{d}S_1,\ \overline{Nu_{\mathrm{r}}}=\frac{\sin\phi}{A}\int_0^{\frac{A}{\sin\phi}}Nu_{\mathrm{r}}\mathrm{d}S_2,$$

where $\mathrm{d}S_1$ and $\mathrm{d}S_2$ are small element lengths along the left and right walls, respectively. The average Nusselt number ($\overline{Nu}$) is defined by $\overline{Nu}=\frac{1}{2}(\overline{Nu_{\mathrm{l}}}+\overline{Nu_{\mathrm{r}}})$.

2.5 Sherwood number

The mass transfer rate in terms of the local Sherwood number (Sh) is defined by

$$Sh=-\frac{\partial C}{\partial n},$$

where n is the normal direction on a plane. The local Sherwood number at right wall (Sh_{r}) and left wall (Sh_{l}) are given by

$$Sh_{\mathrm{r}}=-\sin\phi\frac{\partial C}{\partial X}+\cos\phi\frac{\partial C}{\partial Y},\quad Sh_{\mathrm{l}}=\sin\phi\frac{\partial C}{\partial X}+\cos\phi\frac{\partial C}{\partial Y}.$$

The average Sherwood number at left and right walls are defined as follows:

$$\overline{Sh_{\mathrm{l}}}=\frac{\sin\phi}{A}\int_0^{\frac{A}{\sin\phi}}Sh_{\mathrm{l}}\mathrm{d}S_1,\quad \overline{Sh_{\mathrm{r}}}=\frac{\sin\phi}{A}\int_0^{\frac{A}{\sin\phi}}Sh_{\mathrm{r}}\mathrm{d}S_2,$$

where $\mathrm{d}S_1$ and $\mathrm{d}S_2$ are small element lengths along the left and right walls, respectively. The average Sherwood number ($\overline{Sh}$) is defined by $\overline{Sh}=\frac{1}{2}(\overline{Sh_{\mathrm{l}}}+\overline{Sh_{\mathrm{r}}})$.

3 Numerical solution procedure

The second-order finite-difference approximation of Eqs. (14), (15), and (19) using Appendix may be rewritten in the matrix form as follows:

$$Q\theta = 0, \tag{20}$$

$$RC = 0, \tag{21}$$

$$S\psi = f\left(Ra,\ Pr,\ Ha,\ U,\ V,\ \theta_\xi,\ C_\xi,\ \psi_\xi,\ \psi_\eta\right), \tag{22}$$

where ψ_ξ and ψ_η can be obtained solving the following equations by Thomas algorithm:

$$(\psi_\xi)_{i+1,j} + 4(\psi_\xi)_{i,j} + (\psi_\xi)_{i-1,j} = \frac{3}{h}(\psi_{i+1,j} - \psi_{i-1,j}), \tag{23}$$

$$(\psi_\eta)_{i,j+1} + 4(\psi_\eta)_{i,j} + (\psi_\eta)_{i,j-1} = \frac{3}{h}(\psi_{i,j+1} - \psi_{i,j-1}). \tag{24}$$

For a grid of size $m \times n$, the coefficient matrices Q, R, and S are of order mn and $\psi,\ \theta,$ C and f are mn-component vectors. We solve this problem using outer–inner iteration procedure as described by Gupta and Kalita (2005). We solve Eqs. (20), (21), and (22) using the biconjugate gradient stabilized (BiCGStab) method which constitutes inner iterations. Once both the Eqs. (20), (21), and (22) are solved, then we solve for ψ_ξ and ψ_η using Thomas algorithm for the tridiagonal linear systems arising from Eqs. (23) and (24). This constitutes one outer iteration cycle. We use same relaxation parameter λ inside both the inner and outer iteration cycles for ψ, θ, and C. After calculating ψ_ξ and ψ_η, we compute U and V from Eq. (18). The computations were stopped when the maximum ψ error, θ error, and C error between two successive outer iteration steps were smaller than 0.5×10^{-6}.

4 Results and discussion

In the present study, we simulate double-diffusive convection flow due to both the thermal and solutal effects in a trapezoidal cavity filled with water-based nanofluid. The effects of volume fraction of nanoparticles, type of nanoparticles, Rayleigh number, and Hartmann number on fluid flow, heat transfer characteristics, and solutal transfer characteristics in the cavity are discussed in terms of streamlines, isotherms, isoconcentrations, average Nusselt numbers, and average Sherwood numbers. Prandtl number in the present paper is considered to be 0.7.

4.1 Code validation and grid independence study

Our code is validated by comparing the results with the benchmark results of Basak et al. (2012) and Davis (1982) when pure working fluid is used in the square cavity ($\phi = 90°$) for different values of Rayleigh number and $Pr = 0.71$ as shown in Table 2. In addition, validation of present results with those of Ghasemi et al. (2011) for $\psi_{\min}$ is given in Table 3 using 81×81 grids. It is observed from these tables that our results agree very well with those of the previous researchers' results.

The grid independence test is done using different grid sizes within trapezoidal enclosure with different aspect ratios ($A = 0.5$, 1) and is presented in Table 4 for $Ra = 10^6$, $Ha = 40$, $N = -2$, $Le = 1$, $\phi = 60°$, and $\varphi = 0.05$. Considering various grids 21×21, 41×41, 81×81 and 161×161, thus we conclude that 81×81 grid is enough for all the calculations.

Table 2 Code validation for $|\psi_{\max}|$ and average Nusselt number ($\overline{Nu}$)

Ra	Basak et al. (2012)		Davis (1982)		Present	
	$\lvert\psi_{\max}\rvert$	$\overline{Nu}$	$\lvert\psi_{\max}\rvert$	$\overline{Nu}$	$\lvert\psi_{\max}\rvert$	$\overline{Nu}$
10^3	1.1746	1.1179	–	1.118	1.1733	1.1173
10^4	5.0737	2.2482	–	2.243	5.0739	2.2482
10^5	9.6158	4.5640	9.612	4.519	9.6211	4.5158

Table 3 Code validation for $\psi_{\min}$

Ha	Ghasemi et al. (2011)			Present		
	0	30	60	0	30	60
$Ra = 10^3$	− 0.95	− 0.11	− 0.03	− 0.9552	− 0.1130	− 0.0299
$Ra = 10^5$	− 11.44	− 5.66	− 2.47	− 11.4353	− 5.6712	− 2.4773

Table 4 Grid independence test for $|\psi_{\max}|$

A	$\lvert\psi_{\max}\rvert$			
	21 × 21	41 × 41	81 × 81	161 × 161
0.5	7.0155	6.9688	6.9622	6.9618
1	13.2434	13.3110	13.3287	13.3228

4.2 Effects of Hartmann number

The effects of the Hartmann number on the streamlines, isotherms, and isoconcentrations are presented in Fig. 3a–c, respectively, for $Ra = 10^6$, $Le = 1$, $A = 0.5$, $N = -2$, $\phi = 60°$. The enclosure is filled with a water-based Al_2O_3 nanofluid, which has solid volume fraction φ= 0.03. The buoyancy-driven circulating flows within the enclosure are evident for all values of the Hartmann numbers. The strength of these circulations decreases as the value of Hartmann number increases. This is evident from the fact that the maximum value of stream function in an enclosure decreases with the increase in strength of the magnetic field which is the effect of Lorentz force. It means that as strength of magnetic field increases, conduction mode of heat transfer becomes dominant to convection mode of heat transfer. The maximum values of ψ are 8.48, 6.9, 4.74, and 3.21 for $Ha = 0$, 40, 80, and 120, respectively. The results also show a conduction-dominated regime with vertical isotherms and isoconcentrations at high Hartmann number and a convection-dominated regime with horizontal isotherms and isoconcentrations at low Hartmann number. The isotherms and isoconcentrations are affected by variations in the Hartmann number. These effects are more noticeable at $Ha = 0$ and 40, where an increase in the Hartmann number results in the change of path of isotherms and isoconcentrations from horizontal to vertical. This is an indication of weaker convection flows at higher Hartmann number. Figure 4a, b shows how the average Nusselt number and average Sherwood number, respectively, vary with the Hartmann number at different values of the solid volume fraction ($0 \leq \varphi \leq 0.1$), for $Ra = 10^6$, where the heat and mass transfer are only due to conduction. The average Nusselt number and average Sherwood number decrease when the Hartmann number increases. In addition, the average Nusselt number and average Sherwood number decrease when the volume friction of the nanofluid increases. In

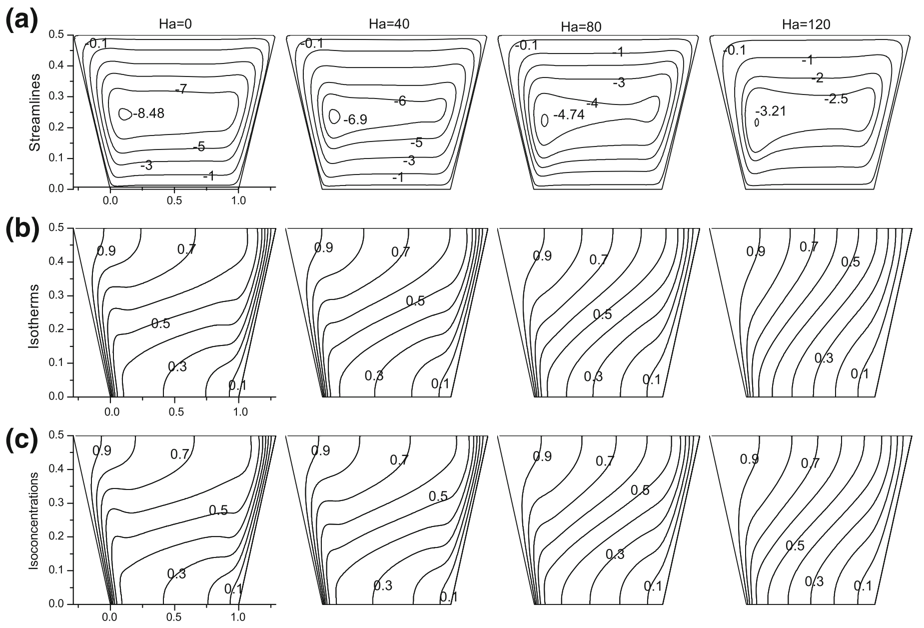

Fig. 3 Effects of Hartmann number (Ha) **a**stream function (ψ), **b** isotherms (θ), and **c** isoconcentrations (C) for $Le = 1$, $A = 0.5$, $N = -2$, $Ra = 10^6$, and $\varphi = 0.03$, $\phi = 60°$

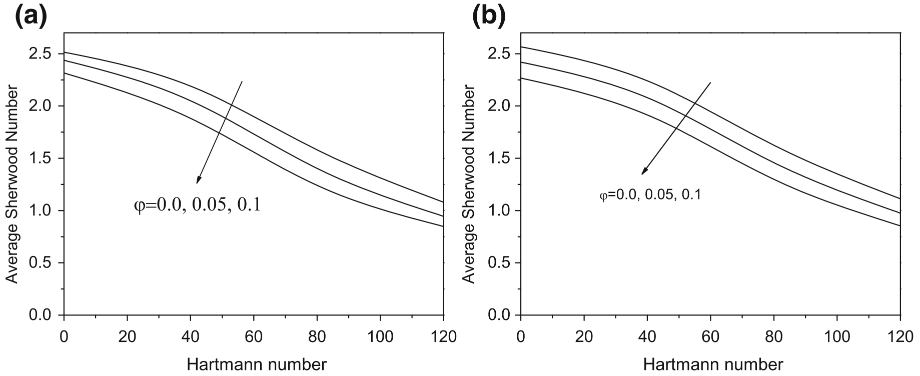

Fig. 4 Effects of Hartmann number (Ha) versus **a** average Nusselt number, and **b** average Sherwood number for $Le = 1$, $A = 0.5$, $N = -2$, $Ra = 10^6$, $0 \leq \varphi \leq 0.1$, and $\phi = 60°$

fact, the increase in volume friction (φ) means that more nanoparticles were added in the base fluid which makes the nanofluid more viscous which in turn slowdown the fluid movement.

4.3 Effects of inclination angle

The effects of inclination angle on the streamlines, isotherms, and isoconcentrations are presented in Fig. 5a–c, respectively, for $Ra = 10^6$, $Le = 1$, $A = 1$, $N = -2$, and $Ha = 40$. The enclosure is filled with a water-based Al_2O_3 nanofluid, which has a solid volume fraction $\varphi = 0.03$. The buoyancy-driven circulating flows within the enclosure are evident for all values

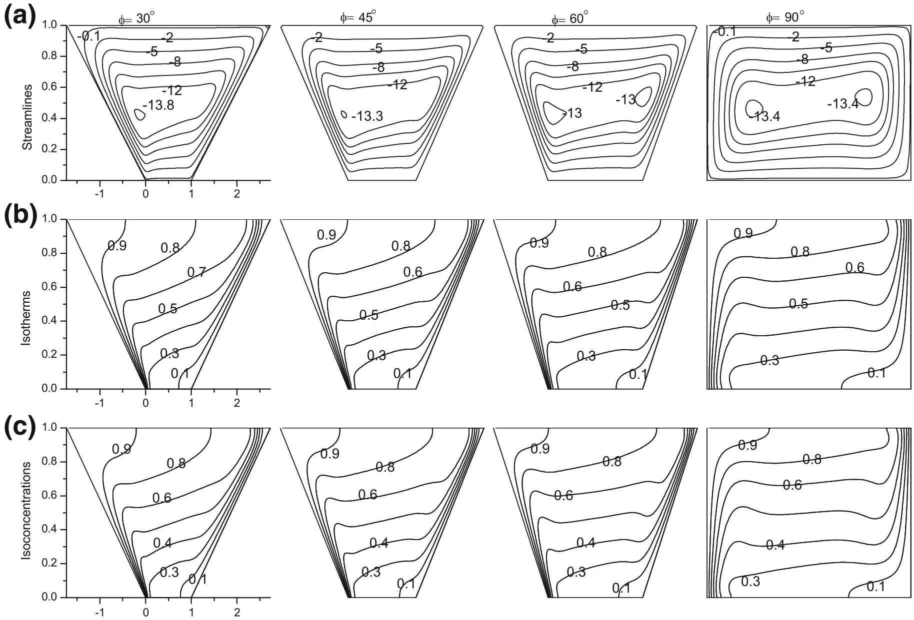

Fig. 5 Effects of inclination angle (ϕ): **a** stream function (ψ), **b** isotherms (θ), and **c** isoconcentrations (C) for $Le = 1$, $A = 1$, $N = -2$, $Ra = 10^6$, and $\varphi = 0.03$, $Ha = 40$

of inclination angles of a trapezoidal cavity. The strength of circulation (the maximum values of ψ) decreases as $\phi = 30°$ is increased 60°, buts when ϕ is increase from 60° to 90°, the strength of this circulation increases. When inclination angle (ϕ) is more than 45° nature of heat transfer becomes less convective but more conductive and so the curvature of streamline is reduced. As observed from Fig. 5, the inclination angle (ϕ) of the cavity has an important role on the eddy strength. It is interesting to note two circulation (smallest) zones exist for $\phi = 60°$ and 90°. The maximum values of ψ are 13.8, 13.3, 13, and 13.4 for $\phi = 30°$, 45°, 60° and 90°, respectively. Comparing Figs. 3a and 5a for $Ha = 40$, the maximum values of ψ increase with the increase in A. From Fig. 4b, c it is evident that the isotherms and isoconcentrations are affected by variations of inclination angle (ϕ), i.e., the line of isotherms and isoconcentrations in the core of the cavity tends to be horizontal as inclination angle increased. Figure 6a, b shows how the average Nusselt number and average Sherwood number, respectively, vary with inclination angle at different values of the solid volume fractions ($0 \leq \varphi \leq 0.1$), for fixed values of other parameters. The average Nusselt number and average Sherwood number are increased when the inclination angle is increased. The average Sherwood number decreases when the volume fraction of nanofluid increases. For small values of inclination angle, moreover, average Nusselt number decreases when volume fraction nanoparticles (φ) increases, but, for more than a certain value of inclination angle, the opposite trend is observed.

4.4 Effects of aspect ratio

The effects of the aspect ratio on the streamlines, isotherms, and isoconcentrations are presented in Fig. 7a–c, respectively, for $Ra = 10^6$, $Le = 1$, $Ha = 40$, $N = -10$, $\phi = 60°$,

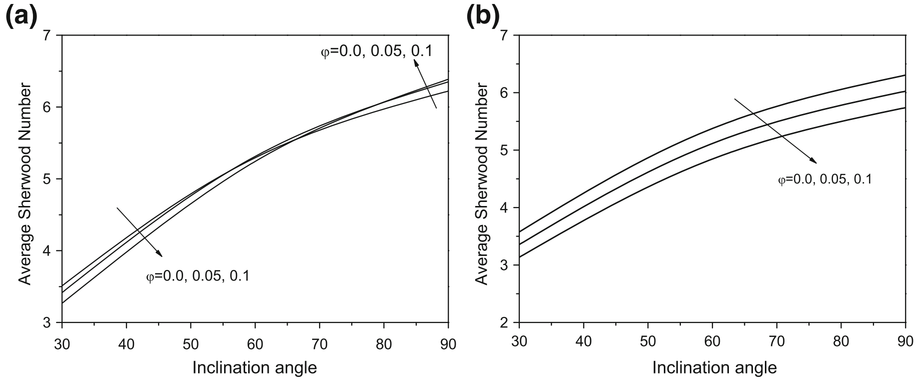

Fig. 6 Effects of inclination angle (ϕ) versus **a** average Nusselt number, and **b** average Sherwood number for $Le = 1$, $A = 1$, $N = -2$, $Ra = 10^6$, $0 \le \varphi \le 0.1$, and $Ha = 40$

and $\varphi = 0.03$, when water-based Al_2O_3 nanofluid is used. The buoyancy-driven circulating flows within the enclosure are evident for all values of the aspect ratio. The strength of these circulations increases as aspect ratio increases. Actually, once the Rayleigh number, Ra, is assigned, the increase of the cavity aspect ratio is obtained by increasing volume of the cavity. This implies that the resistance encountered by the fluid to flow across the cavity increases, and, consequently, due to the increase in the volume fraction of the nanofluid effective viscosity starts becoming excessive in comparison with the growth of the effective thermal conductivity at a larger aspect ratio. The maximum values of ψ are 7.76, 20.4, 27, and 33.2 for $A = 0.5$, 1, 1.5, and 2, respectively. Comparing Figs. 3a and 7a, it is seen that, for $A = 0.5$, $Ha = 40$, the maximum strength (ψ) of these circulations increases with the decrease in values of N. Also one small circulation zone exists for $N = -2$, but two small circulation zone exists for $N = -10$. The results also show a conduction-dominated regime with vertical isotherms at a small value of $A (= 0.5)$ and a convection-dominated regime with horizontal isotherms and isoconcentrations at high aspect ratio ($1 \le A \le 2$). The large values of A, the isotherms, and isoconcentrations remain horizontal. Figure 8a, b, respectively, shows how the average Nusselt number and average Sherwood number vary with aspect ratio (A) for various values of the solid volume fraction ($0 \le \varphi \le 0.1$). The average Nusselt number and average Sherwood number increase when aspect ratio increases. It is seen that the Sherwood number, a measure of rate of mass transfer, is optimized at the highest Ra and lowest A for both base fluid and nanofluid. In addition, mass transfer rate is more effective for nanofluid than the base fluid. This mitigation of heat transfer is mainly attributed to the effective dynamic viscosity which is predominant in the natural convection of nanofluid for low effective thermal conductivity. In addition, the average Nusselt number almost remains unchanged when the volume fraction of nanofluid increases.

4.5 Effects of Rayleigh number

Figure 8a–c illustrate streamlines (ψ), isotherms (θ), and isoconcentrations (C) for various values of Ra. The strength of these circulations increases as the Ra increases. As Ra increases, the strength of fluid flow increases and that leads to increase in thermal energy transport due to enhanced convection. This happens due to the fact that increasing buoyancy force causes natural convection in the cavity with the increase of Rayleigh number. The

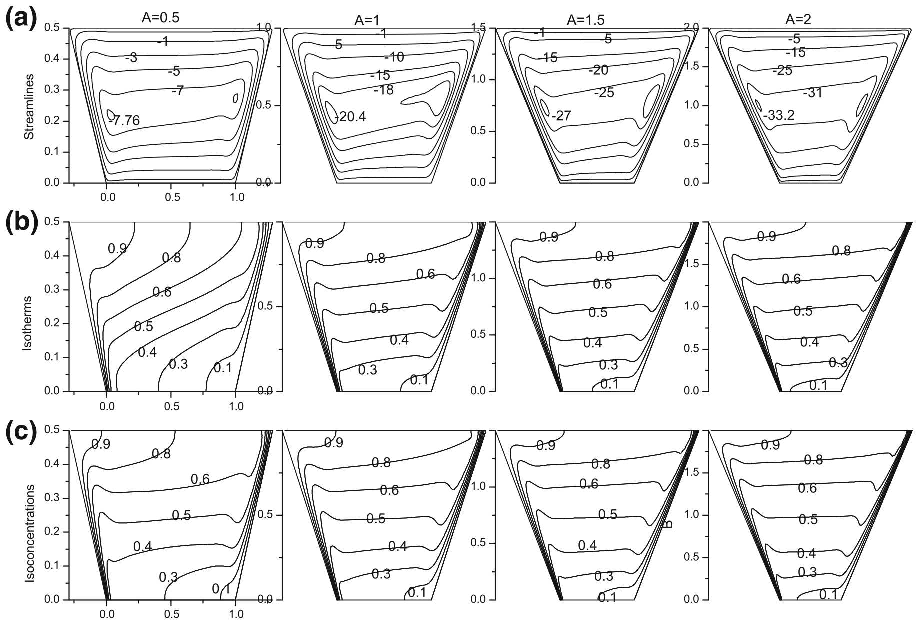

Fig. 7 Effects of aspect ratio (A) **a** stream function (ψ), **b** isotherms (θ), and **c** isoconcentrations (C) for $Le = 1$, $\phi = 60°$, $N = -10$, $Ra = 10^6$, and $\varphi = 0.03$, $Ha = 40$

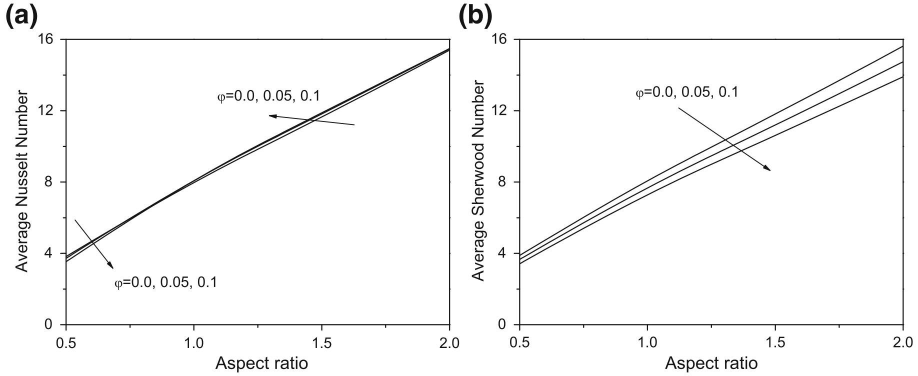

Fig. 8 Effects of aspect ratio (A) versus **a** average Nusselt number and **b** average Sherwood number for $Le = 1$, $\phi = 60°$, $N = -10$, $Ra = 10^6$, $0 \leq \varphi \leq 0.1$, and $Ha = 40$

maximum values of ψ are 1.58, 6.9, and 16.75 for $Ra = 10^5$, 10^6, and 10^7, respectively. Comparison of Figs. 5a and 9a shows that, as the aspect ratio increases from 0.5 to 1, the maximum value of ψ increases for $Ra = 10^6$. It is also noted that, when the aspect ratio $A = 0.5$, single small circulation zone exists, but, for the aspect ratio $A = 1$, two small circulation zones exist. Comparing Figs. 7a and 8a, it is seen that, when N increases from -10 to -2, the maximum values of ψ increase for $Ra = 10^6$, $A = 0.5$, and $Ha = 40$. The results also show a conduction-dominated regime with almost vertical isotherms and isoconcentrations at low $Ra(= 10^5)$ and a convection-dominated regime with almost horizontal isotherms and isoconcentrations at high $Ra(= 10^7)$. Comparison of Figs. 7c and 9c

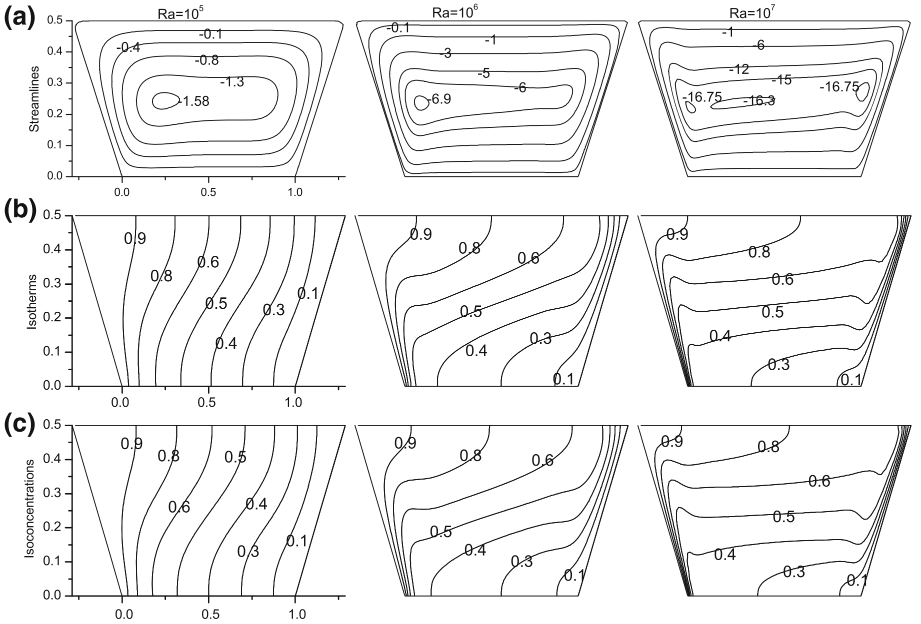

Fig. 9 Effects of Rayleigh (Ra) **a** stream function (ψ), **b** isotherms (θ), and **c** isoconcentrations (C) for $Le = 1$, $\phi = 60°$, $N = -2$, $A = 0.5$, $\varphi = 0.03$, and $Ha = 40$

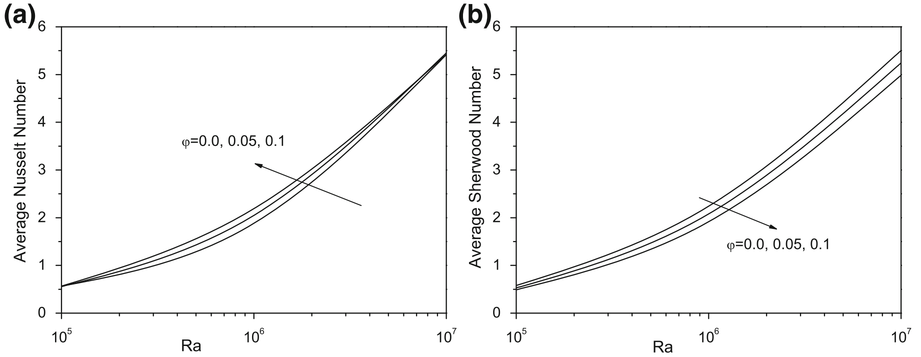

Fig. 10 Effects of Rayleigh (Ra) versus **a** average Nusselt number, and **b** average Sherwood number for $Le = 1$, $\phi = 60°$, $N = -2$, $A = 0.5$, $0 \leq \varphi \leq 0.1$, and $Ha = 40$

shows that, as N increases, the pattern of isoconcentrations remains almost horizontal but the pattern of isoconcentrations remains almost vertical for $Ra = 10^6$, $A = 0.5$, $Ha = 40$, $\varphi = 0.03$, $Le = 1$, and $\phi = 60°$. Figure 10a, b shows that the average Nusselt number and average Sherwood number, respectively, vary with Ra for different values of the solid volume fraction ($0 \leq \varphi \leq 0.1$). The average Nusselt number and average Sherwood number increase with increasing the value of Ra. It is interesting to note that if the solid volume fraction of water-based Al_2O_3 nanofluid increases, then average Nusselt number increases, but average Sherwood number decreases. It is found that the addition of nanoparticles has an effect on the average Nusselt number, indicating a better heat transfer. In addition, the effect of the nanoparticles is more significant at low Rayleigh number than at high Rayleigh number.

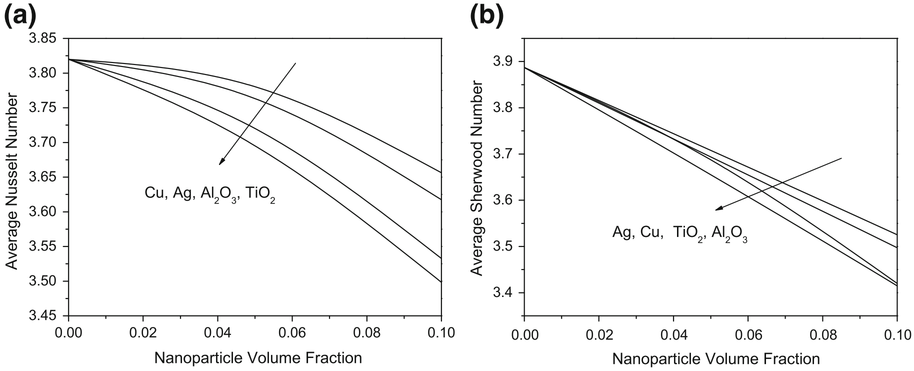

Fig. 11 Average Nusselt number (left) and average Sherwood number (right) versus volume fraction for different nanoparticles, $Le = 1$, $A = 0.5$, $N = -10$, $Ra = 10^6$, and $\phi = 60°$

4.6 Effects of nanoparticles

Finally, variations of average Nusselt number and average Sherwood number with nanoparticle volume fraction for different kinds of nanoparticles consisting of Cu, Ag, Al_2O_3, and TiO_2 are compared in Fig. 11a, b. It can be seen from these figures that, for nanoparticles with larger thermal conductivity, the average Nusselt number and average Sherwood number are large. In other words, by increasing the value of volume fraction, both the average Nusselt number and average Sherwood number are decreased. For the same physical conditions, the minimum solutal transfer occurs when Al_2O_3 or TiO_2 nanoparticles with small thermal conductivity are used and the maximum heat transfer occurs when Ag or Cu nanoparticles with large thermal conductivity are used.

5 Conclusion

Fluid flow, and heat and mass transfer in a trapezoidal cavity filled with water-based nanofluid with different inclination angle (ϕ), aspect ratio (A), magnetic field parameter (Ha), and Rayleigh number (Ra) are studied. The main findings can be summarized as follows:

- The recirculation eddy in the cavity is reduced as the magnetic field strength increases which results in decrease of the convection heat transfer. In such case, conduction heat transfer becomes dominant.
- The maximum values of ψ, average Nusselt number and average Sherwood number increase when the value of A increases keeping other parameters fixed.
- The convective heat transfer is an increasing function of Rayleigh number, and hence, the mass transfer also follows this fashion.
- Increasing Hartmann number has the opposite effect than that of increasing Rayleigh number. Higher Hartmann number weakens convection for both nanofluid and base fluid. However, nanofluid provides higher value of the average Nusselt number than base fluid even when magnetic field is applied.
- The maximum value of ψ increases for ($30° \leq \phi \leq 60°$) and decreases for ($60° \leq \phi \leq 90°$) for increasing values of ψ when other parameters are fixed.

- In addition, we see that the average Nusselt number decreases when we use Cu, Ag, Al_2O_3, and TiO_2 as nanoparticles and the lowest value of the average Nusselt number was obtained for TiO_2 nanoparticle. This can be justified by the fact that TiO_2 nanoparticle has less thermal conductivity compared to the other type of nanoparticles.

Acknowledgements One of the authors, T. R. Mahapatra, is thankful to the University Grant Commission, New Delhi, India, for providing the financial support through SAP (DRS PHASE III) [Sanction letter no. F. 510/3/DRS-III/2015 (SAP)].

Appendix

$$
\begin{aligned}
P_1 &= \frac{\mu_{\mathrm{nf}}}{\rho_{\mathrm{nf}}\alpha_{\mathrm{f}}},\quad P_2 = \frac{\sigma_{\mathrm{nf}}\rho_{\mathrm{f}}}{\sigma_{\mathrm{f}}\rho_{\mathrm{nf}}}Ha^2,\quad P_3 = \frac{(\rho\beta)_{\mathrm{nf}}}{\rho_{\mathrm{nf}}\beta_{\mathrm{f}}}RaPr,\quad P_4 = \frac{\alpha_{\mathrm{nf}}}{\alpha_{\mathrm{f}}},\\
B &= UG + 0.5VEA - H\,P_4,\ P_6 = UG + 0.5VEA - \frac{H}{Le},\\
G &= \frac{1}{1+2\eta A\cot\phi},\quad E = -\frac{2G\cot\phi(2\xi-1)}{A},\quad F = G^2[1+\cot^2\phi(2\xi-1)^2],\\
H &= 4G^2\cot^2\phi(2\xi-1),\quad M = -UG + VG(2\xi-1)\cot\phi + P_1H,\\
T_1 &= -8P_1FG^2(1-2\xi)\cot^2\phi + P_1FH\\
&\quad + FM - 4AG^3\cot\phi[1+(1-2\xi)^2\cot^2\phi],\\
T_2 &= -\frac{8}{A}P_1FG\cot\phi - 8P_1EG^2(1-2\xi)\cot^2\phi\\
&\quad + P_1EH - \frac{8}{A}G^3P_1\cot\phi[1+(1-2\xi)^2\cot^2\phi] + ME - \frac{VE}{A},\\
T_3 &= -\frac{4}{A}P_1EG\cot\phi - \frac{8}{A^2}P_1G^2(1-2\xi)\cot^2\phi + \frac{P_1H}{A^2} + \frac{M}{A^2} - \frac{VE}{A},\\
T_4 &= 24G^2P_1\cot^2\phi + 32P_1EG^3A(1-2\xi)\cot^3\phi\\
&\quad + 24G^4P_1\cot^2\phi[1+(1-2\xi)^2\cot^2\phi]\\
&\quad - 4MG^2(1-2\xi)\cot^2\phi + MH + 4VG^3\cot\phi[1+(1-2\xi)^2\cot^2\phi],\\
T_5 &= \frac{2P_1F}{A^2} + P_1E^2,\\
T_6 &= 16G^2P_1E\cot^2\phi + \frac{32}{A}P_1G^3(1-2\xi)\cot^3\phi - \frac{4}{A}MG\cot\phi\\
&\quad + \frac{4}{A}VG^2(1-2\xi)\cot^2\phi - \frac{VH}{A},\\
T_7 &= -32P_1EG^3A\cot^3\phi - 96P_1G^4(1-2\xi)\cot^4\phi\\
&\quad + 8MG^2\cot^2\phi - 16VG^3(1-2\xi)\cot^3\phi,\\
\frac{\partial\psi}{\partial\xi} &= \frac{1}{2h}(\psi_{i+1,j} - \psi_{i-1,j}) + O(h^2),\\
\frac{\partial\psi}{\partial\eta} &= \frac{1}{2h}(\psi_{i,j+1} - \psi_{i,j-1}) + O(h^2),\\
\frac{\partial^2\psi}{\partial\xi^2} &= \frac{1}{h^2}(\psi_{i+1,j} - 2\psi_{i,j} + \psi_{i-1,j}) + O(h^2),
\end{aligned}
$$

$$
\begin{aligned}
\frac{\partial^2\psi}{\partial\eta^2} &= \frac{1}{h^2}(\psi_{i,j+1} - 2\psi_{i,j} + \psi_{i,j-1}) + O(h^2),\\
\frac{\partial^2\psi}{\partial\xi\partial\eta} &= \frac{1}{4h^2}(\psi_{i-1,j-1} - \psi_{i+1,j-1} + \psi_{i+1,j+1} - \psi_{i-1,j+1}) + O(h^2),\\
\frac{\partial^3\psi}{\partial\xi^2\partial\eta} &= \frac{1}{2h^3}(2\psi_{i,j-1} - 2\psi_{i,j+1} - \psi_{i-1,j-1}\\
&\quad -\psi_{i+1,j-1} + \psi_{i+1,j+1} + \psi_{i-1,j+1}) + O(h^2),\\
\frac{\partial^3\psi}{\partial\xi^3} &= \frac{1}{h^2}(\psi_{\xi i+1,j} - 2\psi_{\xi i,j} + \psi_{\xi i-1,j}) + O(h^2),\\
\frac{\partial^3\psi}{\partial\eta^3} &= \frac{1}{h^2}(\psi_{\eta i,j+1} - 2\psi_{\eta i,j} + \psi_{\eta i,j-1}) + O(h^2),\\
\frac{\partial^3\psi}{\partial\xi\partial\eta^2} &= \frac{1}{2h^3}[2\psi_{i-1,j} - 2\psi_{i+1,j} - \psi_{i-1,j-1}\\
&\quad +\psi_{i+1,j-1} + \psi_{i+1,j+1} - \psi_{i-1,j+1}] + O(h^2),\\
\frac{\partial^4\psi}{\partial\xi^4} &= \frac{6}{h^4}[h(\psi_{\xi i+1,j} - \psi_{\xi i-1,j}) - 2(\psi_{i+1,j} - 2\psi_{i,j} + \psi_{i-1,j})] + O(h^2),\\
\frac{\partial^4\psi}{\partial\eta^4} &= \frac{6}{h^4}[h(\psi_{\eta i,j+1} - \psi_{\eta i,j-1}) - 2(\psi_{i,j+1} - 2\psi_{i,j} + \psi_{i,j-1})] + O(h^2),\\
\frac{\partial^4\psi}{\partial\xi^3\partial\eta} &= \frac{1}{2h^3}[2\psi_{\xi i,j-1} - 2\psi_{\xi i,j+1} - \psi_{\xi i-1,j-1}\\
&\quad -\psi_{\xi i+1,j-1} + \psi_{\xi i+1,j+1} + \psi_{\xi i-1,j+1}] + O(h^2),\\
\frac{\partial^4\psi}{\partial\xi\partial\eta^3} &= \frac{1}{2h^3}[2\psi_{\eta i-1,j} - 2\psi_{\eta i+1,j} - \psi_{\eta i-1,j-1}\\
&\quad +\psi_{\eta i+1,j-1} + \psi_{\eta i+1,j+1} - \psi_{\eta i-1,j+1}] + O(h^2),\\
\frac{\partial^4\psi}{\partial\xi^2\partial\eta^2} &= \frac{1}{h^4}[4\psi_{i,j} - 2(\psi_{i-1,j} + \psi_{i+1,j} + \psi_{i,j-1} + \psi_{i,j+1}) + \psi_{i-1,j-1}\\
&\quad +\psi_{i+1,j-1} + \psi_{i+1,j+1} - \psi_{i-1,j+1}] + O(h^2).
\end{aligned}
$$

Here, h is the step length on a uniform rectangular mesh in the transformed domain.

References

Arani AAA, Kakoli E, Hajialigol N (2014) Double-diffusive natural convection of Al_2O_3-water nanofluid in an enclosure with partially active side walls using variable properties. J Mech Sci Technol 28(11):4681–4691

Arefmanesh A, Aghaei A, Ehteram H (2015) Mixed convection heat transfer in a CuO-water filled trapezoidal enclosure effects of various constant and variable properties of the nanofluid. Appl Math Model 000:1–17

Basak T, Roy S, Singh SK, Pop I (2009) Finite element simulation of natural convection within porous trapezoidal enclosures for various inclination angles: Effect of various wall heating. Int J Heat Mass Transf 52:4135–4150

Basak T, Kumar P, Anandalakshmi R, Roy S (2012) Analysis of entropy generation minimization during natural convection in trapezoidal enclosures of various angles with linearly heated side walls. Ind Eng Chem Res 51:4069–4089

Brinkman HC (1952) The viscosity of concentrated suspensions and solution. J Chem Phys 20:571–581

Chen S, Liu H, Zheng CG (2012) Numerical study of turbulent double-diffusive natural convection in a square cavity by LES-based lattice Boltzmann model. Int J Heat Mass Transf 55:4862–4870

Chen S, Yang Bo, Luo Kai H, Xiong X, Zheng C (2016) Double diffusion natural convection in a square cavity filled with nanofluid. Int J Heat Mass Transf 95:1070–1083

Corcione M (2010) Heat transfer features of buoyancy-driven nano fluids inside rectangular enclosures differentially heated at the side walls. Int J Therm Sci 49:15–36

Das MK, Oha PS (2009) Natural convection heat transfer augmentation in a partially heated and partially cooled square cavity utilizing nanofluids. Int J Numer Methods Heat Fluid Flow 19:411–431

Dastmalchi M, Sheikhzadeh GA, Arani AAA (2015) Double diffusive natural convective in a porous square enclosure filled with nanofluid. Int J Therm Sci 95:88–98

Davis GD (1982) Natural convection of air in a square cavity: a bench mark numerical solution. Int J Numer Methods Fluids 3:249–264

Esfahani JA, Bordbar V (2011) Double diffusive natural convection heat transfer enhancement in a square enclosure using nanofluids. J Nanotechnol Eng Med 2:1–9

Ghasemi B, Aminossadati SM, Raisi A (2011) Magnetic field effect on natural convection in a nanofluid-filled square enclosure. Int J Therm Sci 50:1748–1756

Gupta MM (1975) Discretization error estimates for certain splitting procedures for solving first biharmonic boundary value problems. SIAM J Numer Anal 12:364–377

Gupta MM, Kalita JC (2005) A new paradigm for solving NavierStokes equations: streamfunction-velocity formulation. J Comput Phys 207:52–68

Kalita JC, Sen S (2012) The biharmonic approach for unsteady flow past an impulsively started circular cylinder. Commun Comput Phys 12(4):1163–1182

Kefayati G (2015) FDLBM simulation of mixed convection in a lid-driven cavity filled with non-Newtonian nanofluid in the presence of magnetic field. Int J Therm Sci 95:29–46

Lyiean L, Bayazitoglu Y, Witt LC (1980) An analytical study of natural convection heat transfer within a trapezoidal enclosure. J Heat Transf 102:640–647

Mahapatra TR, Pal D, Mondal S (2013) Mixed convection flow in an inclined enclosure under magnetic field with thermal radiation and heatgeneration. Int Commun Heat Mass Transf 41:47–56

Mahmoodi M (2011) Numerical simulation of free convection of nanofluid in a square cavity with an inside heater. Int J Therm Sci 50:2161–2175

Mahmoudi AH, Abu-Nada E (2013) Combined effect of magnetic field and nanofluid variable properties on heat transfer enhancement in natural convection. Numer Heat Transf 63:452–472

Nasrin R, Parvin S (2012) Investigation of buoyancy-driven flow and heat transfer in a trapezoidal cavity filled with water-Cu nanofluid. Int Commun Heat Mass Transf 39:270–274

Nayak RK, Bhattacharyya S, Pop I (2015) Numerical study on mixed convection and entropy generation of Cu-water nanofluid in a differentially heated skewed enclosure. Int J Heat Mass Transf 85:620–634

Pal D, Mandal G (2015) MHD convective stagnation-point flow of nanofluids over a non-isothermal stretching sheet with induced magnetic field. Meccanica 50(8):2023–2035

Pal D, Mandal G, Vajravalu K (2014) Convective- radiation effect on stagnation-point flow of nanofluids over a stretching/shrinking surface with viscous dissipation. J Mech 30(3):289–297

Pal D, Mandal G, Vajravalu K (2015) Mixed convection stagnation-point flow of nanofluids over a stretching/shrinking sheet in a porous medium with internal heat generation/absorption. Commun Numer Anal 1:30–50

Pandit SK (2008) On the use of compact streamfunction-velocity formulation of steady Navier-Stokes equations on geometries beyoud rectangular. J Sci Comput 36:219–242

Parvin S, Nasrin R, Alim MA, Hossain NF (2013) Double diffusive natural convection in a partially heated cavity using nanofluid: an aanlysis. Glob Sci Tech J 1(1):123–134

Peric M (1993) Natural convection in trapezoidal cavity. Int J Numer Heat Transf 24:213–219

Sheremet MA, Oztop HF, Pop I, Abu-Hamdeh N (2016) Analysis of entropy generation in natural convection of nanofluid inside a square cavity having hot solid block: Tiwari and Das Model. Entropy 18(9):1–15

Sivasankaran S, Kandaswamy P (2006) Double diffusive convection of water in a rectangular partitioned enclosure with temperature dependent species diffusivity. Int J Fluid Mech Res 33(4):345–361

Teamah MA, Shehata Ali I (2016) Magnetohydrodynamic double diffusive natural convection in trapezoidal cavities. Alexandria Eng J 55:1037–1046

Tofaneli LA, de Lemos MJS (2009) Double-diffusive turbulent natural convection in a porous square cavity with opposing temperature and concentration gradients. Int Commun Heat Mass Transf 36:991–995

Uddin MB, Rahman MM, Khan MAH, Saidur R, Ibrahim TA (2016) Hydromagnetic double-diffusive mixed convection in trapezoidal enclosure due to uniform and nonuniform heating at the bottom side: Effect of Lewis number. Alexandria Eng J 55:1165–1176

Xuan Y, Roetzel W (2000) Conceptions for heat transfer correlation of nanofluids. Int J Heat Mass Transf 43(19):3701–3707